Influence of nonmagnetic Zn substitution on the lattice and magnetoelectric dynamical properties of the multiferroic material CuO

S. P. P. Jones,[1] N. C. Wurz,[2] M. Failla,[2] D. Prabhakaran,[1] C. F. McConville,[2] and J. Lloyd-Hughes[2,*]

[1]*University of Oxford, Department of Physics, Clarendon Laboratory, Parks Road, Oxford OX1 3PU, United Kingdom*

[2]*University of Warwick, Department of Physics, Gibbet Hill Road, Coventry CV4 7AL, United Kingdom*

(Received 2 June 2014; revised manuscript received 22 July 2014; published 7 August 2014)

Dynamic magnetoelectric coupling in the improper ferroelectric $Cu_{1-x}Zn_xO$ ($x = 0$, $x = 0.05$) was investigated using terahertz time-domain spectroscopy to probe electromagnon and magnon modes. Zinc substitution was found to reduce the antiferromagnetic ordering temperature and widen the multiferroic phase, under the dual influences of spin dilution and a reduction in unit-cell volume. The impact of Zn substitution on lattice dynamics was elucidated by Raman and Fourier-transform spectroscopy, and shell-model calculations. Pronounced softenings of the A_u phonons, active along the direction of ferroelectric polarization, occur in the multiferroic state of $Cu_{1-x}Zn_xO$, and indicate strong spin-phonon coupling. The commensurate antiferromagnetic phase also exhibits spin-phonon coupling, as evidenced by a Raman-active zone-folded acoustic phonon, and spin dilution reduces the spin-phonon coupling coefficient. While the phonon and magnon modes broaden and shift as a result of alloy-induced disorder, the electromagnon is relatively insensitive to Zn substitution, increasing in energy without widening. The results demonstrate that electromagnons and dynamic magnetoelectric coupling can be maintained even in disordered spin systems.

DOI: 10.1103/PhysRevB.90.064405 PACS number(s): 75.85.+t, 78.30.−j

I. INTRODUCTION

Multiferroics display multiple hysteretic orders, such as ferroelectricity, ferromagnetism, or ferroelasticity [1,2]. Abundant possibilities for multiferroics include novel solid-state memories, photovoltaics [3], spin valves [4], sensors, and actuators [5]. Magnetically induced improper ferroelectrics, typified by $TbMnO_3$ [6], have strong magnetoelectric (ME) coupling but small polarizations only at cryogenic temperatures ($\lesssim 1\ \mu C\ cm^{-2}$ at <70 K), as the microscopic interactions that induce polarization are relatively weak [2]. Cupric oxide (CuO) exhibits an incommensurate magnetic phase between $T_{N1} = 213$ K and $T_{N2} = 230$ K that is ferroelectric [7]. Hydrostatic pressure has recently been suggested to enhance T_{N2} theoretically, while simultaneously broadening the width in temperature of the multiferroic phase [8]. This offers the prospect of magnetically induced ferroelectricity at room temperature.

The static polarization of improper ferroelectric multiferroics such as $RMnO_3$ (R: rare earths) can be understood as arising from the spin current [9] or Dzyaloshinskii-Moriya (DM) interaction [10], where spin-orbit coupling produces a polarization proportional to the cross product of adjacent spins ($\mathbf{S}_i \times \mathbf{S}_j$). By contrast, the dynamic response under oscillating electric fields E_ω and magnetic fields H_ω can elucidate other significant interactions that are not necessarily revealed by the static ordering. Electromagnons—spin waves that become electric-dipole active in a magnetoelectric phase—are a recently discovered quasiparticle excitation that provide a window into the important spin interactions of magnetoelectrics [11–17]. The electric-field tuning of electromagnons in $DyMnO_3$, an improper ferroelectric multiferroic [18], and of magnons in bulk $BiFeO_3$, a proper ferroelectric multiferroic [19], establish the potential of spin waves in data processing and communications [20].

Electromagnons have been discovered in improper ferroelectric multiferroics such as $RMnO_3$ and RMn_2O_5 at low temperature (<70 K) [11–17], and between 213 and 230 K in CuO [21]. Two prominent models of electromagnons are discussed in the literature, with different microscopic origins. (1) *Heisenberg electromagnons* are linked to changes in a $\mathbf{S}_i \cdot \mathbf{S}_j$ term in the Hamiltonian [22,23]. A Heisenberg-type electromagnon can be evidenced by the invariance of the electromagnon selection rule when the spin cycloid changes orientation [24]. For instance, the $E_\omega \| a$ selection rule for electromagnons in $TbMnO_3$ is not altered [24] when the spin cycloid flops from the bc to the ab plane for $B > 5$ T. Here, the high-frequency mode corresponds to an electrically active zone-edge magnon, and a lower frequency mode to a similar mechanism involving folding of the Brillouin zone caused by magnetic modulation of the cycloid [23,24]. Additional terms in the spin Hamiltonian such as single-ion anisotropy and biquadratic exchange are required to model spectral features of electromagnons in the manganites [25]. (2) *Dzyaloshinskii-Moriya electromagnons* are eigenmodes of spin cycloids, and permit ac electric fields to couple directly to cycloids induced by the DM interaction [14,26]. A DM electromagnon has been reported in $TbMnO_3$, substantially weaker than the Heisenberg electromagnons [16]. The electric-field control of polarization of terahertz (THz) radiation has recently been demonstrated using DM electromagnons in $DyMnO_3$ [18].

Electromagnons may permit novel THz optical components, such as chromatic filters, wave plates, or directionally dichroic filters [27]. Room-temperature, tunable electromagnons (under readily accessible electric or magnetic fields) are therefore strongly desired. Increasing the ferroelectric ordering temperature T_{N2} of CuO may provide a route to electromagnons at room temperature. While hydrostatic pressures may broaden the width of the multiferroic phase of CuO above room temperature [8], chemical pressure via

*j.lloyd-hughes@warwick.ac.uk

 ©2014 American Physical Society

alloying is a more attractive route technologically. Moreover, it has been suggested that alloying with nonmagnetic ions could cause the multiferroic phase to be stabilized at higher temperatures [28].

In this paper an investigation is reported of the influence of alloying with nonmagnetic zinc ions upon the multiferroic state of CuO. Terahertz time-domain spectroscopy revealed that the energy of the electromagnon excitations in $Cu_{1-x}Zn_xO$ increased when $x = 0.05$. The presence of electromagnons in single-crystal and polycrystalline samples indicated that the multiferroic phase was preserved. A greater reduction in T_{N1} in comparison to T_{N2} created a broadening of the multiferroic state, which is discussed in the context of spin-dilution and alloy-induced lattice distortions. Spin-lattice coupling in $Cu_{1-x}Zn_xO$ was further investigated by examining phonon modes using Fourier transform infrared (FTIR) spectroscopy, Raman spectroscopy, and lattice dynamics calculations.

After providing background information about the phases of CuO in Sec. II, growth details and a structural characterization are reported in Sec. III. The magnon and electromagnon excitations of $Cu_{1-x}Zn_xO$ are discussed in Sec. IV, and the dynamic lattice response is detailed in Sec. V. The influence of alloying on lattice dynamics are discussed in Sec. VI with the aid of lattice dynamics calculations, and a discussion of spin dilution in quasi-one-dimensional spin chains is provided. Conclusions are drawn in Sec. VII.

II. BACKGROUND: CUPRIC OXIDE

The magnetic phases of CuO have previously been studied using neutron diffraction [29,30]. At low temperatures there is a commensurate, collinear antiferromagnetic phase (AF1) with two Cu^{2+} sublattices with spins aligned along the b axis. The strongest antiferromagnetic (AFM) superexchange interaction J_1 occurs along spin chains in the $[10\bar{1}]$ direction. Weaker ferromagnetic (FM) coupling exists between chains on the same sublattice in the [101] and [010] directions [31]. Intersublattice coupling is of similar magnitude to the FM coupling and leads to the stabilisation of the spin spiral phase above $T_{N1} = 213$ K. In the multiferroic AF2 phase, between T_{N1} and T_{N2}, spins on one sublattice flop into the ac plane [29,30,32], and an incommensurate spin spiral structure is formed with magnetic modulation vector $\mathbf{Q} = (0.006,0,0.017)$. The spin structure is essentially a cycloid, with a small (proper) screw component [7]. This phase exhibits a static electric polarization $\sim 100\ \mu C\ m^{-2}$ along b [7,33,34] that is not significantly altered in magnetic fields up to 16 T [35], suggesting weak static magnetoelectric coupling in CuO. The multiferroic phase does, however, exhibit switching of magnetic domains under an electric field [34]. Further, CuO shows a sizable dynamic magnetoelectric response, with an electromagnon in the ME phase that was recently discovered using terahertz time-domain spectroscopy (THz-TDS) [21].

Numerous studies have been made on polycrystalline CuO alloyed with various ions, including heterovalent ions [36–38] Li^+, Fe^{3+}, and Ga^{3+}, and homovalent ions [37–41] Mn^{2+}, Fe^{2+}, Co^{2+}, Ni^{2+}, and Zn^{2+}. However, none of these studies were made after the discovery (in 2008) that the AF2 magnetic phase drives improper ferroelectricity [7].

III. GROWTH AND CHARACTERIZATION

Single crystals of CuO and $Cu_{0.95}Zn_{0.05}O$ were prepared from high-purity (>99.999%) powders of CuO and ZnO. Cylindrical rods were sintered at 950 °C for three days under oxygen flow. Single crystals were grown using an optical floating-zone furnace under a high-pressure oxygen atmosphere [42]. Samples were cut from the boule and oriented by Laue diffraction, resulting in 1.3-mm-thick single-crystal samples with the following in-plane orientations and diameters ϕ: CuO with $\phi = 1.8$ mm, (101) and $(10\bar{1})$; CuO with $\phi = 6$ mm, (101) and (010); $Cu_{0.95}Zn_{0.05}O$ with $\phi = 2$ mm, (101) and $(10\bar{1})$; $Cu_{0.95}Zn_{0.05}O$ with $\phi = 3$ mm, (101) and (010). Polycrystalline samples were prepared with larger diameters ($\phi = 8$ mm), and thickness 2 mm. Susceptibility versus temperature loops from superconducting quantum interference device (SQUID) magnetometry on single-crystal samples (from the same growth as used in this study) exhibited anomalies at $T_{N1} \simeq 160$ K and $T_{N2} \simeq 200$ K for $x = 0.05$, and at $T_{N1} = 213$ K and $T_{N2} \simeq 230$ K for CuO [42]. While ferroelectric polarization loops were measured by the pyroelectric current method for $x = 0$ [34], resistive losses at room-temperature prevented pyroelectric measurements at $x = 0.05$.

High-resolution x-ray powder diffraction was used to examine the crystal structure at room temperature. Pieces of single crystal were ground to a fine powder and pressed into pellets before characterization using a powder x-ray diffractometer (PANalytical X'pert Pro) with a Cu $K\alpha$ source and monochromator. A Rietveld refinement was performed using the TOPAS software package. The space group of CuO ($C2/c$) was unchanged on alloying with Zn, resulting in the unit-cell parameters presented in Table I. No new diffraction peaks associated with the single-phase alloyed material were seen, supporting the space-group assignment. Weak peaks indicating the presence of small amounts of unreacted ZnO were detected. A clear increase in a, decrease in b, a negligible change in c, and an increase in β are all in good agreement with the trend reported by Arbuzova *et al.* [37] for up to 3% Zn.

The structural changes induced by Zn alloying may produce subtle changes in the superexchange interaction strengths. For instance, the calculated Cu-O-Cu bond angle in the $[10\bar{1}]$ direction (AFM order, strongest J) increases slightly upon Zn substitution, as reported in Table I.

TABLE I. Summary of the structural properties of $Cu_{1-x}Zn_xO$ from Rietveld analysis of powder XRD data, compared with results from Åsbrink and Norrby [43]. Experiments were performed at 300 K. V denotes the unit-cell volume, while $\theta_{[10\bar{1}]}$ is the Cu-O-Cu bond angle in the $[10\bar{1}]$ direction.

	CuO[a]	CuO	$Cu_{0.95}Zn_{0.05}O$	Change on alloying
a (Å)	4.6837	4.6835	4.7116	+0.68%
b (Å)	3.4226	3.4277	3.4027	−0.73%
c (Å)	5.1288	5.1313	5.1308	−0.01%
β (°)	99.54	99.48	99.90	+0.42%
V (Å^3)	81.08	81.25	81.03	−0.27%
$\theta_{[10\bar{1}]}$ (°)	146.48	146.43	146.84	+0.28%

[a]Data from Åsbrink and Norrby.

It is interesting to note that the effect of replacing 5% of Cu with Zn is to decrease the unit-cell volume V, a similar influence to pressure [8], although alloying does not introduce an isotropic change in a, b, and c. Using the DFT predictions of Rocquefelte *et al.* (Ref. [8]), a hydrostatic pressure of 150 MPa would reduce the unit-cell volume by the same fraction as 5% zinc substitution.

The change in V can be discussed in the context of the ionic radii of Cu^{2+} and Zn^{2+}. Ionic radii are commonly quoted based on tabulated values for ions with a coordination number $N = 6$ (octahedral coordination). However, in cupric oxide the Cu^{2+} ions are coordinated with four coplanar oxygen ions situated at the corners of an almost regular parallelogram, due to a strong Jahn-Teller distortion. The oxygens are coordinated by four Cu^{2+} ions situated at the corners of a distorted tetrahedron [43]. The "crystal radii" from Shannon and Prewitt [44,45] are therefore appropriate for tetrahedrally coordinated O^{2-} ions, and square-planar Cu^{2+} ions in CuO, rather than the "effective ionic radii," which are calculated based on octahedrally coordinated ions. While Cu^{2+} and Zn^{2+} radii for $N = 6$ are 0.87 and 0.89 Å respectively, square-planar coordinated Cu^{2+} with $N = 4$ has a crystal radius of 0.76 Å. There is no value for square-planar coordinated Zn^{2+} and no Jahn-Teller effect in this ion, which has a full $3d$ orbital. For a tetrahedrally coordinated Zn^{2+} ion ($N = 4$) the crystal radius is 0.74 Å suggesting that it would be perfectly reasonable for the effective radius to decrease when Zn^{2+} replaces Cu^{2+} in the CuO lattice, leading to a reduced unit-cell volume, concurring with the x-ray-diffraction results reported in Table I. The partially covalent nature of bonding in $Cu_{0.95}Zn_{0.05}O$ may also play a role, rather than considering ionic bonding alone, as in the preceding discussion.

IV. DYNAMIC MAGNETOELECTRIC RESPONSE

A. Terahertz time-domain spectroscopy

The low-energy spin excitations of $Cu_{1-x}Zn_xO$ were probed by terahertz time-domain spectroscopy (THz-TDS) [46] in the energy range 0.8–12.4 meV, for sample temperatures from 2 to 300 K. A wide-area GaAs photoconductive switch and a ZnTe electro-optic crystal were used to generate and detect single-cycle pulses of THz radiation transmitted through the samples. THz-TDS directly determines the amplitude of the electric field E_ω after interaction with the sample, providing knowledge of the complex refractive index $\tilde{n} = n + i\kappa$. Using linearly polarized THz radiation and a variety of single crystals with different orientations the contributions to $\tilde{n}$ from each optical axis were determined independently, and modes were identified as electric-dipole active (electromagnons) or magnetic-dipole active (magnons) [47], as discussed in the following sections.

B. Results: Electromagnon

The THz absorption coefficient $\alpha = 2\omega\kappa/c$ for a single-crystal $Cu_{0.95}Zn_{0.05}O$ [oriented with $E_\omega \parallel (101)$ and $H_\omega \parallel (010)$] is reported in Fig. 1(a) for different temperatures. A monotonic increase in α with energy is observed for temperatures below 159.5 K and above 190 K, as evidenced by the dash-dotted curve for $T = 159.0$ K. This increase in

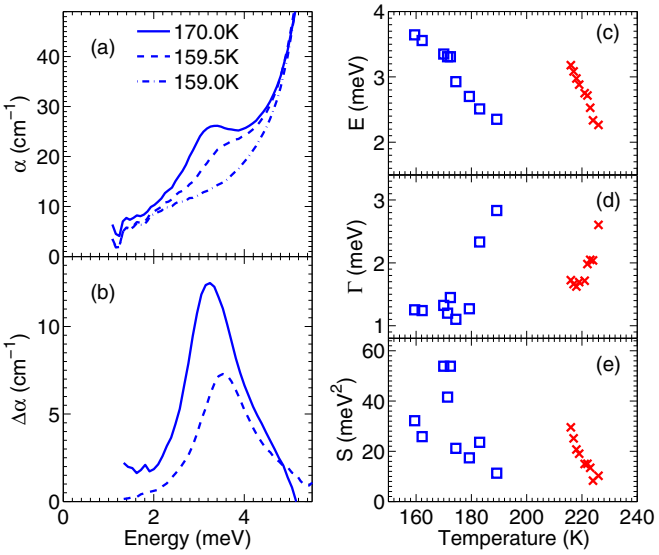

FIG. 1. (Color online) (a) THz absorption coefficient α measured for $Cu_{0.95}Zn_{0.05}O$ with $E_\omega \parallel (101)$ and $H_\omega \parallel (010)$ for temperatures 159.0 K (dash-dotted line), 159.5 K (dashed line), and 170.0 K (solid line). The onset of the electromagnon absorption resonance around 3 meV is clear at $T = 159.5$ K. (b) Relative absorption $\Delta\alpha(T) = \alpha(T) - \alpha(T_0)$ for $Cu_{0.95}Zn_{0.05}O$ with $T_0 = 159.0$ K and $T = 159.5$ K (dashed line) and $T = 170.0$ K (solid line). (c) Energy E, (d) linewidth Γ, and (e) oscillator strength S of the electromagnon for $x = 0.05$ (blue points, left) and $x = 0$ (red points, right). E lowers, Γ diverges, and S decreases as the temperature rises towards $T_{N2} = 190$ K ($x = 0.05$) or $T_{N2} = 230$ K ($x = 0$).

α results from the IR-active phonons for $E_\omega \parallel (101)$ (B_u^1, B_u^2, and B_u^3; Sec. V). Zinc alloying modifies the IR-active phonons of CuO, as discussed in Sec. V, and produces an enhanced absorption of THz radiation above 4 meV for $x = 0.05$ in comparison to $x = 0$.

At $T = 159.5$ K (dashed line) a clear resonant absorption feature emerges around 3 meV, which redshifts and strengthens at $T = 170.0$ K (solid line). The change in absorption coefficient $\Delta\alpha(T) = \alpha(T) - \alpha(T_0)$ is shown in Fig. 1(a) to elucidate the changes in α with respect to $T_0 = 159.0$ K, for $T = 159.5$ K (dashed line) and $T = 170.0$ K (solid line). This absorption mode was assigned as an electromagnon as no such feature was present for $E_\omega \parallel (010)$ (same crystal) or $E_\omega \parallel (10\bar{1})$ [(010)-oriented crystal] and regardless of the direction of H_ω, as found for the pure material [21]. Therefore the $E_\omega \parallel (101)$ electromagnon selection rule is preserved on alloying, and the change in $\tilde{n} = \sqrt{\tilde{\epsilon}\tilde{\mu}}$ can be ascribed to a change in the dielectric function $\tilde{\epsilon}$ rather than the permittivity $\tilde{\mu}$.

To extract the temperature dependence of the electromagnon resonance the change in absorption coefficient was modelled by a single Lorentzian oscillator with an added linear term (which accounts for the low-frequency tail of the broad higher lying phonons), as discussed in detail in Ref. [21]. The extracted electromagnon energies are plotted in Fig. 1(c) for $x = 0.05$ in comparison to $x = 0$. The electromagnon is uniquely present in the multiferroic state of CuO, from $T_{N1} = 213$ K to $T_{N2} = 230$ K, and between $T_{N1} = 159.5$ K and $T_{N2} = 190$ K for $x = 0.05$. These values are consistent with the

lower and upper temperatures of the incommensurate magnetic phase, as witnessed by the magnetic susceptibility [42]. A significant rise in the electromagnon energy at T_{N1} from 3.1 meV in CuO to 3.7 meV in $Cu_{0.95}Zn_{0.05}O$ can be seen. The linewidth Γ of the electromagnon is only weakly affected by alloying with Zn, with comparable values for $x = 0$ and $x = 0.05$. Γ can be seen to diverge in Fig. 1(d) when $T \rightarrow T_{N2}$. The oscillator strength $S = \Delta\epsilon E^2$ is reported in Fig. 1(e) for $Cu_{1-x}Zn_xO$, where $\Delta\epsilon$ is the difference between the high-frequency and low-frequency dielectric constant above and below the resonance energy E. S is comparable at T_{N1} for $x = 0$ and $x = 0.05$. The onset of electromagnon absorption is within 0.5 K for $Cu_{1-x}Zn_xO$ at T_{N1}, and S reduces towards zero at T_{N2}.

C. Results: Magnon

In pure CuO a magnon excitation at 6.6 meV at 10 K, with linewidth $\leqslant$0.1 meV, has previously been observed by THz-TDS [21]. This magnon was active when $H \parallel (101)$, and only in the commensurate AF1 magnetic phase of CuO. In the present study an absorption feature was observed at 3 meV in the commensurate state, as pictured in Figs. 2(a) and 2(b) at 4 K (solid lines) and 20 K (dashed lines). The mode can be seen in Fig. 2(c) to be at the same energy for $H_\omega \parallel (101)$, $E_\omega \parallel (010)$ ($\square$ symbols) and $H_\omega \parallel (101)$, $E_\omega \parallel (10\bar{1})$ ($\circ$ symbol). The $H \parallel (101)$ selection rule (independent of the direction of E_ω) implies that this mode is also a magnon, obeying the same selection rule as the 6.6-meV magnon in CuO.

The temperature dependence of the magnon mode energy is reported in Fig. 2(c) by the $\square$ symbols for $Cu_{1-x}Zn_xO$, and weakly increases in E with temperature until the mode disappears at around 70 K. In comparison, the energy of the observed magnon in CuO was found to decrease as the temperature increased towards T_{N1} [+ symbols in Fig. 2(c)], and in accordance with a simple model of the sublattice magnetization [21]. The stronger absorption above 4 meV for $x = 0.05$ prohibited verification of whether the 6.6-meV magnon ($x = 0$, 10 K) was present in the Zn-alloyed samples. The width Γ of the 3-meV magnon for $x = 0.05$ is substantially broader than that of the magnon in pure CuO ($\Gamma \leqslant 0.1$ meV at 10 K). At present it is unclear whether the 3-meV mode for $x = 0.05$ is the same spin excitation as seen at 6.6 meV in CuO [21], or if it is in fact related to the 1.2-meV mode seen in electron spin resonance (ESR) measurements on CuO [$\square$ in Fig. 2(c)] [48]. Neutron or ESR experiments on $Cu_{1-x}Zn_xO$ are needed to clarify this situation.

It is interesting to note that the 3-meV magnon in $Cu_{0.95}Zn_{0.05}O$ is not visible for $T \geqslant 70$ K, well below $T_{N1} = 159.5$ K, while the higher-lying magnon in CuO persists to $T_{N1} = 213$ K. This may indicate a different origin for these two modes.

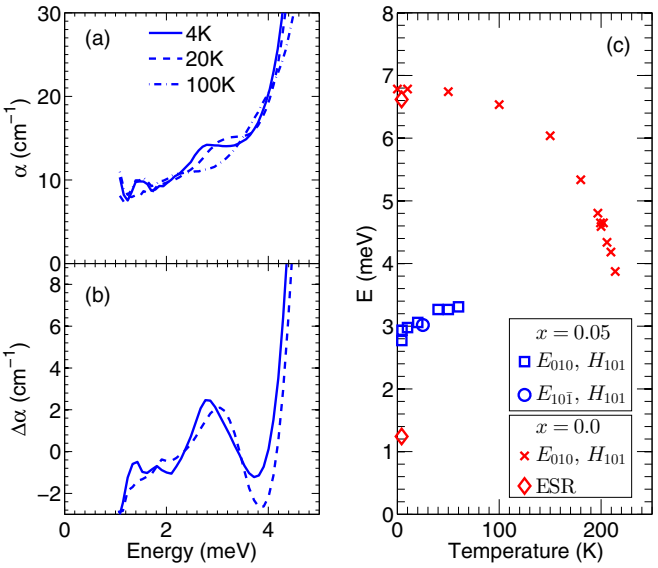

FIG. 2. (Color online) Magnon resonances in $Cu_{1-x}Zn_xO$. (a) Absorption α is shown for selected temperatures for a $Cu_{0.95}Zn_{0.05}O$ crystal with $H_\omega \parallel (101)$, $E_\omega \parallel (010)$. (b) Relative absorption $\Delta\alpha = \alpha(T) - \alpha(T_0)$ with $T_0 = 100$ K showing the magnon mode around 3 meV. (c) Magnon energies for $Cu_{1-x}Zn_xO$ vs temperature. Data are presented for $x = 0.05$ for $H_\omega \parallel (101)$, $E_\omega \parallel (010)$ (blue $\square$) and $H_\omega \parallel (101)$, $E_\omega \parallel (10\bar{1})$ (blue $\circ$). Magnon energies for CuO from electron-spin resonance measurements (red $\diamondsuit$) [48], and THz-TDS (red $\times$) [21] are also shown.

V. DYNAMIC LATTICE RESPONSE

A. Symmetry analysis

The predicted lattice vibrations of CuO allowed by symmetry have been established in the literature. A factor group analysis assuming the centrosymmetric $C2/c$ space group, and using the tables of Rousseau *et al.* (Ref. [49]), gives the following representation:

$$\Gamma_{CuO} = A_g \oplus 2B_g \oplus 4A_u \oplus 5B_u. \quad (1)$$

The primitive unit cell of CuO contains two formula units giving $3N = 12$ phonon modes. Three of the modes correspond to acoustic phonons ($A_u + 2B_u$) which have zero frequency at the Brillouin-zone center, leaving nine remaining active phonons. In a centrosymmetric crystal none of the principal phonon modes are both infrared and Raman active, and therefore three Raman active modes ($A_g + 2B_g$) and six infrared active modes ($3A_u + 3B_u$) are expected for CuO. The symmetry analysis is presumed to be unchanged for $Cu_{0.95}Zn_{0.05}O$, as the XRD results reported in Sec. III are consistent with space group $C2/c$. The assignment of phonon modes below is therefore based on existing literature for pure CuO. The relative atomic displacements of the zone-center phonons have been calculated previously [50].

B. FTIR and Raman spectroscopy

Fourier-transform infrared (FTIR) spectroscopy was performed in the energy range 10–1000 meV and between 77 and 300 K using a Bruker Vertex 70v spectrometer with a cryostat insert (Oxford Instruments). Near-normal incidence (11°) unpolarized reflectivity spectra were recorded on all samples. A globar light source was used with a KBr beamsplitter and DLaTGS detector in the mid-IR range (40–1000 meV). The far-IR measurements (10–90 meV) used a Si beamsplitter and DTGS detector. Polarization-resolved measurements in the 77–300-K temperature range were performed on ($10\bar{1}$)-oriented $Cu_{1-x}Zn_xO$, using a nitrogen cryostat with polythene windows. A wire-grid polarizer set the polarization to $E_\omega \parallel b$

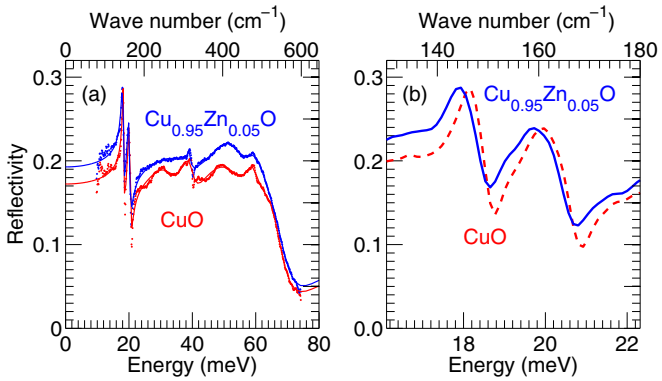

FIG. 3. (Color online) (a) Measured reflectivity of polycrystalline samples of CuO (red points) and $Cu_{0.95}Zn_{0.05}O$ (blue points). A sum of six Lorentzian oscillators (solid lines), as described in the text, models the reflectivity. (b) Experimental reflectivity in the frequency range of the A_u^1 and B_u^1 modes for CuO (red dashed line) and $Cu_{0.95}Zn_{0.05}O$ (blue line).

in order to examine the three A_u phonons, since the A_u^3 mode in particular is thought to show strong spin-phonon coupling in the AF2 phase of pure CuO [51].

A Raman microscope (Renishaw inVia Reflex) in a backscattering geometry was used to measure the Raman shift in the energy range 25–400 meV after exciting with a $\lambda = 633$-nm HeNe laser. A wide-angle 50× objective lens was used to focus and collect the light. A nitrogen-cooled temperature stage (Linkham THM S600) was used for measurements in the range 90–300 K, and a helium-flow cryostat (Oxford Instruments Microstat) for the range below 90 K. Polarization-resolved measurements in the $z(xx)\bar{z}$ and $z(xy)\bar{z}$ geometry were performed on $Cu_{1-x}Zn_xO$ single crystals with the incident beam direction $z \parallel (010)$ (a and c in the plane) or $z \parallel (10\bar{1})$ (b and (101) in the plane).

C. Results: IR-active phonons

All six IR-active phonons of $Cu_{1-x}Zn_xO$ were characterized by FTIR reflectivity measurements on both single-crystal and polycrystalline samples. Representative room-temperature reflectivity spectra are shown in Fig. 3(a) on polycrystalline samples with $x = 0$ and $x = 0.05$. Experimental data (points) were modelled by a dielectric function containing six Lorentzians, following Ref. [51], which reported a polarized FTIR study of single crystals with various orientations. Fitting was performed using the REFFIT software package [52], which uses a Levenberg-Marquardt least-squares fitting algorithm, producing the lines in Fig. 3(a). The obtained phonon energies are summarized in Table II, and are in good agreement with the literature for pure CuO [51]. The error in each fitting parameter was estimated as follows. The chosen parameter was increased, allowing the other parameters to relax each time, until χ^2 increased by 10% from its global minimum. This provides a useful estimate of the error in each parameter.

As evidenced in Table II, alloying in general softens the phonon frequencies, and broadens their linewidth. This finding is discussed in more detail in Sec. VI A. The error in the frequencies of the A_u^2 and $B_u^{2,3}$ modes, determined by the fitting procedure outlined above, is larger, and these modes are broad even in pure CuO. Thus the focus in the following is on the lower frequency IR-active modes, Raman modes, and the A_u^3 mode, which is strongly coupled to the improper ferroelectric phase transition in CuO [51].

The reduction in phonon frequency and broadening upon Zn substitution can be most clearly seen for the sharp, low-frequency A_u^1 and B_u^1 phonons, and the Raman modes. For instance, FTIR reflectivity spectra of the A_u^1 and B_u^1 modes of polycrystalline samples are shown in Fig. 3(b), and show a clear shift to lower frequency after zinc substitution. The A_u^1 mode is an out-of-plane bending mode where O^{2-} ions move in the b direction with Cu^{2+} motion mainly in the ac plane [50].

TABLE II. Summary of the principal phonon energies in $Cu_{1-x}Zn_xO$ in meV (at room temperature), and a spin-coupled X-point Cu LA phonon that is Raman active in the AF1 phase (value reported at 26 K). Results on single-crystal and polycrystalline $Cu_{1-x}Zn_xO$ are compared with results from the literature (polycrystalline CuO: Ref. [53]; single crystals: Ref. [51] for IR-active modes, Refs. [54,55] for Raman-active modes). The errors indicated were determined as described in the main text. Eigenfrequencies from lattice dynamics calculations (Sec. VI A) are shown for the principal Γ-point phonons and the X-point LA phonon that is Raman active by spin-lattice coupling (Sec. V D).

		Polycrystalline			Single crystal			Calculated	
Mode	Activity	CuO[a]	CuO	$Cu_{0.95}Zn_{0.05}O$	CuO[b]	CuO	$Cu_{0.95}Zn_{0.05}O$	CuO	$Cu_{0.95}Zn_{0.05}O$
A_u^1	IR, E$\parallel b$	20.15	20.20 ± 0.07	20.02 ± 0.07	19.90	20.26 ± 0.09	20.12 ± 0.21	19.1	18.7
A_u^2	IR, E$\parallel b$	39.80	39.30 ± 0.62	39.43 ± 0.31	39.86	39.68 ± 0.37	37.4 ± 2.5	40.8	40.1
A_u^3	IR, E$\parallel b$	50.8	52.1 ± 1.9	52.6 ± 1.5	50.7	49.7 ± 1.4	49.2 ± 1.7	51.4	51.5
B_u^1	IR, E$\perp b$	18.23	18.30 ± 0.05	18.09 ± 0.06	17.97	18.35 ± 0.07	18.06 ± 0.15	13.3	12.8
B_u^2	IR, E$\perp b$	59.45	59.0 ± 0.9	60.1 ± 0.7	58.22	59.6 ± 0.6	59.9 ± 1.0	54.6	53.3
B_u^3	IR, E$\perp b$	66.3	64.2 ± 1.7	65.7 ± 2.5	64.8	69.1 ± 0.6	69.6 ± 0.9	80.6	80.2
A_g	Raman				37.19	36.91 ± 0.03	36.27 ± 0.14	25.3	25.1
B_g^1	Raman				42.90	42.89 ± 0.07	42.53 ± 0.12	43.8	43.4
B_g^2	Raman				78.3	78.1 ± 0.7	76.9 ± 0.5	87.0	86.8
LA X	Raman				29.8	29.7 ± 0.01[c]	29.3 ± 0.05[d]	30.3	30.1

[a]From Ref. [53].
[b]From Refs. [51], [54], and [55].
[c]For a (010)-oriented crystal at 26 K.
[d]For a $(10\bar{1})$-oriented crystal at 26 K.

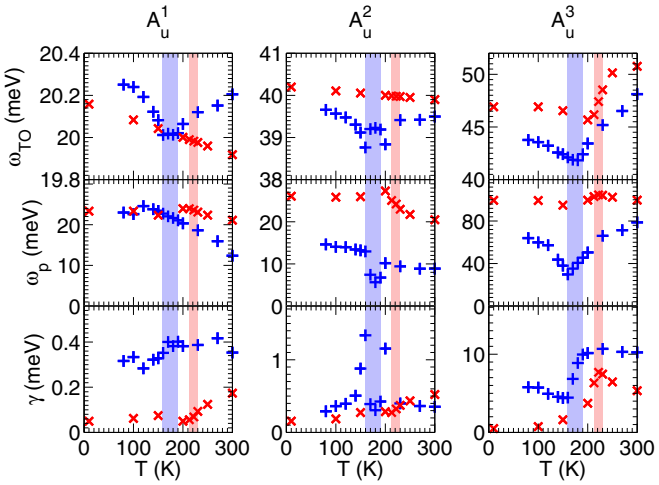

FIG. 4. (Color online) Temperature-dependent parameters for the A_u phonons in $Cu_{0.95}Zn_{0.05}O$ (blue plus symbols, this work) and CuO (red crosses, from Ref. [51]). The temperature ranges of the AF2 incommensurate magnetic phase for $x = 0$ and $x = 0.05$ are shaded. The top, middle, and bottom rows show the mode frequency ω_{TO}, plasma frequency ω_p, and linewidth γ for the three A_u phonons in units of meV. Parameters are extracted from the fits described in the text to polarized $[E_\omega \| (010)]$ FTIR spectra on a single crystal with (010) and (101) in the plane.

The A_u^1 mode softens from 20.20 ± 0.07 meV to 20.02 ± 0.07 meV, while simultaneously broadening from linewidth $\Gamma = 0.7 \pm 0.1$ meV to 0.8 ± 0.2 meV, upon alloying. The B_u^1 mode is complementary, with the O^{2-} motion confined to the *ac* plane with Cu^{2+} ions moving mainly along the *b* axis [50]. This mode lowers from 18.30 ± 0.05 meV to 18.09 ± 0.06 meV while simultaneously broadening from $\Gamma = 0.47 \pm 0.11$ meV to 0.71 ± 0.15 meV.

Polarized FTIR spectra at different temperatures can be used to assess changes in the lattice response upon entering the multiferroic or AFM phases [51]. While most of the IR-active modes are only weakly temperature dependent, the A_u^3 mode of CuO shows an unusually strong temperature dependence. As reported by Kuz'menko *et al.* (Ref. [51]), the oscillator strength and linewidth of the A_u^3 mode are strongly enhanced in and near the incommensurate magnetic phase of CuO. The parameters of the A_u phonons reported in Ref. [51] for $x = 0$ are reproduced in Fig. 4. The A_u^3 mode is active along *b*, parallel to the static polarization in the multiferroic phase. Kuz'menko *et al.* postulated that the A_u^3 mode (at about 51 meV) could couple to two Γ-point magnons each at 23 meV (5.6 THz), as observed by neutron scattering [31].

The temperature-dependent parameters of the A_u modes in $Cu_{1-x}Zn_xO$ with $x = 0.05$ are reported in Fig. 4 in comparison to literature results for $x = 0$. The A_u^1 and A_u^2 mode parameters show small changes in the multiferroic phase (shaded areas), with minima in mode frequencies in the range 160–190 K for $x = 0.05$. In contrast the A_u^3 phonon exhibits a sharp dip in frequency and oscillator strength in the multiferroic phase, accompanied by a step change in the linewidth $\Gamma(T)$. The A_u^3 phonon exhibits the largest *b*-axis oxygen movement of all the IR-active phonons [50], and is thus strongly coupled to ferroelectricity (parallel to *b*) in the incommensurate magnetic phase. The observation that the A_u^3 mode is strongly temperature dependent is evidence that an incommensurate magnetic structure is preserved in $Cu_{1-x}Zn_xO$. The temperature window (160–190 K) for the changes in the A_u modes in $Cu_{1-x}Zn_xO$ coincides with the THz electromagnon reported in Sec. IV.

D. Results: Raman-active phonons

The unpolarized Raman spectra of $Cu_{1-x}Zn_xO$ single crystals [with (101) and (010) in plane] are reported in Figs. 5(a) and 5(b). The principle phonons A_g (♦ symbol), B_g^1 (■), and B_g^2 (▲) redshift in energy *E* and broaden in linewidth Γ on Zn alloying (see also Table II). For instance, on alloying the A_g mode decreases in energy from 36.91 ± 0.02 meV to 36.27 ± 0.15 meV while $\Gamma(A_g)$ increases from 1.41 ± 0.04 meV to 3.5 ± 0.4 meV. Mode assignments were based on polarized Raman spectra (not shown), following results published in the literature [55]. The three principal Raman modes differ from the IR-active modes as only the O^{2-} ions are displaced, and Cu^{2+} sites remain stationary. The A_g phonon is a symmetric breathing mode with motion only

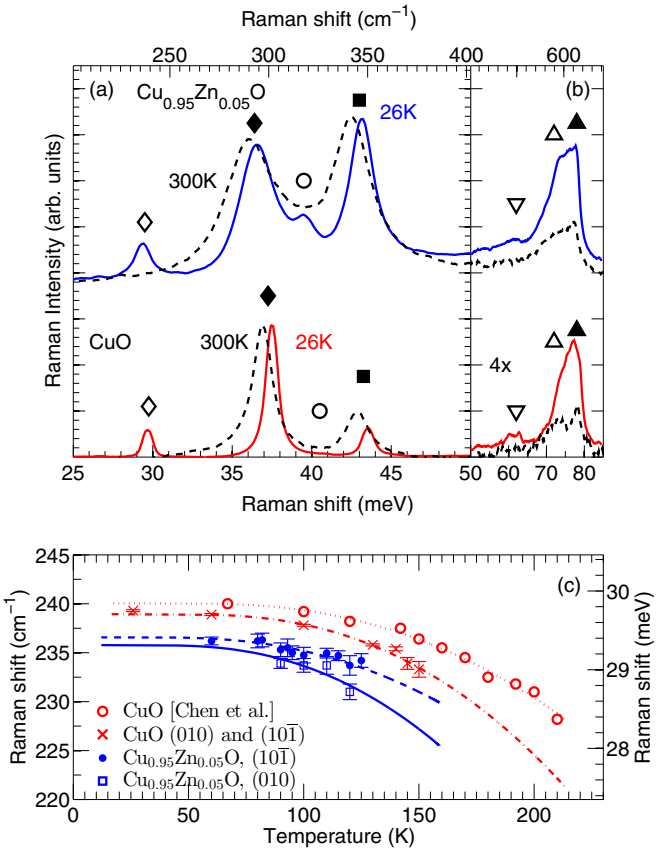

FIG. 5. (Color online) (a),(b) Raman spectra for $Cu_{0.95}Zn_{0.05}O$ (top) and CuO (bottom) at 300 K (dashed lines) and 26 K (solid lines). Note the split *x*-axis scale, and that the data for CuO in (b) have been multiplied by 4. The principal Raman active modes are A_g (♦), B_g^1 (■), and B_g^2 (▲), while additional Raman modes (discussed in the text) are labeled ◊, ○, ▽, and △. (c) Temperature dependence of the zone-folded LA phonon (see text) for *b*-oriented and (10$\bar{1}$)-oriented CuO (crosses), and (10$\bar{1}$) (points) and *b*-oriented (squares) $Cu_{0.95}Zn_{0.05}O$. Circles show data for CuO from Ref. [54].

along the b axis, while the B_g modes involve motion only in the ac plane [50]. The principle phonon modes of $Cu_{1-x}Zn_xO$ narrow and harden on cooling, as a comparison of the solid lines (26 K) and dashed lines (300 K) in Fig. 5 illustrates.

Additional Raman peaks beyond the three predicted by the symmetry analysis are observed in Figs. 5(a) and 5(b) at 29.3 meV (◊), 39 meV (○), 62 meV (▽), and 73 meV (△). Further Raman lines at 142, 289, and 383 meV are also evident for $Cu_{1-x}Zn_xO$ in extended range spectra (not shown). The extra modes can be divided into two distinct groups: (i) those present at all temperatures (modes △, 142 and 289 meV) and (ii) those activated only at low temperature (modes ◊, ○, ▽, 383 meV). None of the additional modes can be attributed to a ZnO impurity phase as all modes are present in both pure and alloyed samples.

Two overlapping peaks (△ and ▲) are evident in Fig. 5(b) around 75 meV, in both the CuO and $Cu_{0.95}Zn_{0.05}O$ Raman spectra. Here B_g^2 is assigned following Choi *et al.* [55] to the higher and broader peak at 78.1 ± 0.7 meV ($x = 0$), which shifts to 76.9 ± 0.5 meV at $x = 0.05$. The second peak (△) is 5.1 meV lower at 73 meV, a splitting that is independent of x and temperature. One possible origin of this peak is the B_u^3 mode (the closest IR-active phonon) if mixed IR and Raman activity is permitted. This would only be the case, however, in a noncentrosymmetric crystal, requiring a different space group than $C2/c$ at all temperatures. An alternative interpretation of this split peak is that the lattice potential may be anharmonic, giving multiple Raman lines [56], or that it results from a multiphonon process. A recent polarization-resolved Raman study on CuO reported that the broad band around 142 meV is a second-order Raman process involving overtones of four relatively dispersionless phonon bands (as determined by DFT) [57]. The 289 meV (present at all temperatures) and 383 meV (appearing below T_{N1}) modes reported here are too high in energy to correspond to first-order Raman scattering from single vibrational modes, and may similarly result from multiphonon processes, or from defects.

Chen *et al.* reported five extra Raman-active modes in the commensurate AF1 state of CuO [54], at 22, 27, 29.3 meV [◊ in Fig. 5(a)], 41 meV (○), and 63 meV (▽). The authors explained these extra modes by a mechanism relying upon Brillouin-zone folding induced by magnetic order. The magnetic unit cell of CuO can be written [58] $\mathbf{a_M} = \mathbf{a} + \mathbf{c}$, $\mathbf{b_M} = \mathbf{b}$, and $\mathbf{c_M} = \mathbf{a} - \mathbf{c}$. The X point of the crystallographic unit cell corresponds to the zone center of the magnetic cell. If the displacement pattern of phonons at X modulates the superexchange interaction, then Raman active modes arise [54]. Chen *et al.* reported that the strongest extra mode, at 29.3 meV (240 cm^{-1}), appears below 210 K. It can also be observed for $Cu_{0.95}Zn_{0.05}O$ in Fig. 5(a) (◊). This mode was previously found [54] to lower in energy for isotopically pure ^{65}CuO in comparison to ^{63}CuO, demonstrating that it results from an LA motion of Cu^{2+} ions along $(10\bar{1})$, modulating the strongest superexchange interaction $J \simeq 80$ meV [31]. The three principal Raman modes were at the same energies for ^{65}CuO and ^{63}CuO, as expected for vibrations associated only with oxygen motion [54], while they shifted to lower frequencies for $Cu^{18}O$ than for $Cu^{16}O$ [59]. Further evidence for the magnetically induced zone folding of phonons in CuO was reported by Kuz'menko *et al.*, who reported additional IR-active modes that were linked to phonon modes at the X and A points [51]. However, it is interesting to note that the extra IR modes were also present above T_{N2}, in the paramagnetic state, where diffuse magnetic scattering persists [58]. A doubling of the unit cell from $\{a,b,c\} \rightarrow \{a+c,b,a-c\}$ was proposed by Kuz'menko *et al.* [51], in line with the magnetic cell.

In Fig. 5(c) the temperature dependence of the X point LA phonon frequency $\omega(T)$ is reported in detail. For the b-oriented and (10-1)-oriented CuO samples studied here the frequency (crosses) is slightly lower than that reported by Chen *et al.* (open circles). For the $Cu_{0.95}Zn_{0.05}O$ samples the $(10\bar{1})$-surface normal sample (filled circles) and the (010) sample (squares) showed even lower frequencies.

Chen *et al.* used an Ising model to derive the temperature dependent phonon frequency when spin-lattice coupling is included, and obtained the expression

$$\omega(T) = \left[\omega_0^2 + 4B'S^2(T)\right]^{1/2}. \quad (2)$$

Here $\omega_0 = \omega(T_{N1})$ is the phonon frequency in the absence of spin-lattice coupling, and the constant B' is linked by $\lambda = -2B'/\omega_0$ to the spin-phonon coupling coefficient λ. The temperature-dependent average value of the spin, $S(T)$, was calculated by assuming that the reduced sublattice magnetization σ obeyed the expression $T/T_{N1} = \sigma/\operatorname{arctanh}(\sigma)$, where $\sigma = 1$ at $T \ll T_{N1}$, $\sigma = 0$ at $T_{N1} = 213$ K (CuO) or $T_{N1} = 159$ K ($Cu_{0.95}Zn_{0.05}O$), and $S(T) = \sigma/2$.

The fits to $\omega(T)$ obtained using Eq. (2) are reported in Fig. 5(c). The dotted line is a fit to the data of Chen *et al.* using $\omega_0 = 228.3$ cm^{-1} and $B' = 5506$ cm^{-2} ($\lambda = -48$ cm^{-1}), while the data reported here for (010)-oriented CuO were modelled by $\omega_0 = 221.4\,cm^{-1}$ and $B' = 8074\,cm^{-2}$ ($\lambda = -73$ cm^{-1}, dash-dotted line). For $Cu_{0.95}Zn_{0.05}O$ $\omega_0 = 229.9$ cm^{-1} and $B' = 3112$ cm^{-2} for the $(10\bar{1})$ sample ($\lambda = -27$ cm^{-1}, dashed line), while $\omega_0 = 225.5$ cm^{-1} and $B' = 4741$ cm^{-2} for the (010)-oriented crystal ($\lambda = -42$ cm^{-1}, solid line). This suggests that spin dilution and the modified unit cell in $Cu_{0.95}Zn_{0.05}O$ lowers the spin-phonon coupling strength, and that crystal orientation appears to play a role [not considered in the simple model of Eq. (2)].

The temperature dependence of $\omega(T)$ was also examined by Shih *et al.*, who found that λ and T_{N1} reduced in CuO nanowires as the diameter decreased [60]. This concomitant reduction in λ with T_{N1} is in line with the findings reported here, and may result from a suppression of long-range antiferromagnetic order induced by dimensionality (Shih *et al.*) or spin disorder (results herein).

VI. DISCUSSION

A. Influence of alloying on phonons

Qualitatively, the substitution of zinc on copper sites will change the effective force constants between neighboring oxygen ions. The addition of an extra d-orbital electron (Cu^{2+} is $3d^9$ and Zn^{2+} is $3d^{10}$) will have the effect of locally eliminating the Jahn-Teller distortion and adding an electron to the orbitals. This will reduce the bonding character of the interactions, effectively reducing the force constants and therefore the phonon frequencies. The enhanced mass of Zn in comparison to Cu should also act to lower IR phonon frequencies for $Cu_{1-x}Zn_xO$.

Phonons soften and broaden upon zinc alloying in the superconductor $YBa_2Cu_{4-x}Zn_xO_8$ [61], which has very similar CuO_4 plaquettes to CuO. A broadened phonon linewidth with increasing alloy fraction has been particularly well studied in Mn-alloyed ZnO, and is successfully described by a spatial correlation model [62,63]. Essentially, the disorder introduced by random (Zn) substitution on the cation sites breaks the translational symmetry of the crystal, thus relaxing the wave-vector $q \approx 0$ selection rule. Now small areas (rather than single points) of the Brillouin zone may be activated by light, allowing phonons of slightly different energies to be excited by photons, and thus broadening the observed linewidth, in accord with the findings in Sec. V.

Quantitative insights into the influence of alloying on phonons can be gained by undertaking lattice dynamics calculations. The principal phonon modes of CuO have been calculated by a number of authors with a variety of approaches including valence force field models [50,53,59,64], core-shell potential models [55,64,65], and DFT [57]. Here the lattice dynamic package GULP [66] was used to calculate the phonon eigenvectors and eigenfrequencies of $Cu_{1-x}Zn_xO$. This approach has the advantages of (i) requiring fewer free parameters than valence force field models (22 parameters in Ref. [64]) and (ii) computational speed and simplicity. Similar to shell models reported previously for CuO [55,64,65] short-range Born-Mayer-Buckingham (BMB) potentials [66] $V(r) = Ae^{-r/\rho} - C/r^6$ between atomic pairs were used to describe interionic interactions at radius r. Cu and O cores were included, and only O ions had polarizable shells as short-range Cu-Cu interactions are weak [64]. Fixed parameters were $A = 22\,764$ eV, $\rho = 0.149$ Å, and $C = 27.88$ eV Å^6 for the O-shell O-shell interionic BMB potential, and $V = kr^2/2$ with $k = 72.94$ eV Å^{-2} for the intraionic O-core O-shell spring potential. Ionic charges were Cu^{+2} for the Cu cores, and $O^{+0.869}$ and $O^{-2.869}$ for the O cores and shells respectively, where the superscripts denote the effective ionic charges in units of the electron charge.

The Cu-core O-shell BMB potential parameters A and ρ were varied (with $C = 0$), in order to fit the experimental Γ-point phonon frequencies ω_{exp} reported in Table II for CuO. The eigenvectors for each calculated phonon frequency were checked to verify mode assignments. The best fit was with $A = 2025.3$ eV and $\rho = 0.2672$ Å, and calculated mode frequencies are reported in Table II, in reasonable agreement with experiment.

The quality of fit was quantified by $\Delta = \hbar \sum |\omega_{\text{exp}} - \omega_{\text{calc}}|/N$ for the $N = 9$ Γ-point modes [64], resulting in $\Delta = 0.35$ meV. Choi *et al.* used $A = 695.4$ eV and $\rho = 0.3372$ Å to fit the Raman-active modes of CuO, producing $\Delta = 0.44$ meV for a relaxed unit cell [55]. In contrast, the shell models of Reichardt *et al.* had $\Delta \simeq 0.053$ meV using $A = 712$ eV and $\rho = 0.300$ Å for the $Cu^{+1.3}$-core $O^{-2.7}$-shell interaction, and $A = 1573$ eV and $\rho = 0.295$ Å for the O-shell O-shell interionic potential. Popov [65] motivated the use of parallel (in-ribbon, i.e., ac plane) and perpendicular (between adjacent ribbons, i.e., b direction) Cu core-O shell parameters, taking into account the Cu-O-Cu ribbons of CuO. Good agreement between calculated phonon dispersion curves and neutron data [64] were found with $A = 1600$ eV, $\rho = 0.2815$ Å for $(Cu^{+3.0}\text{-}O^{-3.0})_{\parallel}$, and $A = 550$ eV, $\rho = 0.2518$ Å for $(Cu^{+3.0}\text{-}O^{-3.0})_{\perp}$. Rather than allowing the effective ionic charges to vary (as in Reichardt *et al.* and Popov's works), here they were fixed: the experimental ionic charge is close to -2 for oxygen [51]. This constraint and the simplicity of our model results in the larger Δ obtained herein. The phonon dispersion curves calculated from our model are also in poorer agreement with experimental results than the simulations of Popov and Reichardt *et al.* [64,65].

To calculate the phonon frequencies of $Cu_{0.95}Zn_{0.05}O$ the same Cu-core O-shell BMB parameters derived for CuO were adopted, and the experimental unit-cell parameters for $Cu_{0.95}Zn_{0.05}O$ were taken. The majority of the eigenfrequencies lowered marginally as a consequence of the structural change. Second, 5% of Cu ions were replaced with Zn ions, and Zn^{+2}-core $O^{-2.869}$-shell BMB parameters $A = 499.6$ eV, $\rho = 0.359$ Å, $C = 0$ were used [67]. This additionally lowered the phonon frequencies, with calculated values reported in Table II. The X-point acoustic-phonon modes were also simulated for $Cu_{1-x}Zn_xO$, one of which (at $\sim$30 meV) involves displacements of Cu ions along the $[10\bar{1}]$ (AFM) direction, in accord with Chen *et al.*'s discussion of the $\sim$29.3 meV mode [54]. A reduction in the calculated frequency upon alloying (Table II) agrees with the experimental results discussed in Sec. V D.

B. Influence of spin dilution on magnetic order

The substitution of a magnetic ion with a nonmagnetic ion has been studied both theoretically and experimentally in systems with different dimensionalities:1D antiferromagnetic spin chains [68] such as TMMC:Cd [69], two-dimensional (2D) Heisenberg antiferromagnets [70,71] and the 3D multiferroic antiferromagnet $MnWO_4$ [72]. The ratio $J_{\text{interchain}}/J_{\text{intrachain}} \sim 10^{-1}$ in CuO [31] indicates that it is weakly 1D in comparison to well studied materials such as TMMC [69], where $J_{\text{interchain}}/J_{\text{intrachain}} \sim 10^{-4}$. CuO is therefore regarded as a quasi-1D collinear Heisenberg antiferromagnet below T_{N1} [73,74]. However, as demonstrated in this section, the effect of alloying on the magnetic ordering temperatures can be described well by a quasi-1D model.

Néel temperatures are suppressed on alloying with nonmagnetic ions, as a consequence of two interrelated effects. Spin dilution due to replacing random spins by nonmagnetic ions affects long-range magnetic correlations. Disorder effects occur because the magnetic superexchange coupling is locally zero around the nonmagnetic ions. These effects are particularly pronounced in quasi-1D systems [68] such as CuO. The correlation length of a group of neighboring spins along a chain increases as the temperature decreases, until the whole crystal is correlated below the magnetic ordering temperature. Nonmagnetic impurities break communication along the chain and restrict the growth of the correlation length to the average impurity separation. Mean-field theory predicts a dramatic decrease in ordering temperature driven by nonmagnetic impurities in a 1D system [68].

A classical Heisenberg model for a quasi-1D system [68] predicts $k_B T_N(x) \simeq k_B T_N(0) - xJ$ in the dilute alloying limit $x \ll k_B T_N(0)/2J \ll 1$. For CuO with an $x = 0.05$ alloy fraction and $J \simeq 80$ meV [31], this predicts $\Delta T_N = T_N(x) - T_N(x = 0.0) = -46$ K. For $J \simeq 70$ meV, $\Delta T_N = -40$ K. The experimentally observed reduction in T_{N2} to 190 K

($\Delta T_N = -40$ K) and T_{N1} to 159 K ($\Delta T_N = -54$ K) at $x = 0.05$ are therefore consistent with dilute spin alloying in a quasi-1D spin chain. However, it should be noted that the Heisenberg J constants will also change in the Zn-alloyed sample as a consequence of the altered crystal structure and Cu-O-Cu bond angles (Table I).

Furthermore, the widening of the AF2 phase with respect to the AF1 phase has been hinted at in the work of Henley, who calculated that if disorder is introduced in a vector antiferromagnet with competing interactions a noncollinear spin state can be stabilized with respect to a collinear state [75]. Evidence supporting this exists in the form of optical-pump x-ray-probe experiments on CuO at 207 K [76]. At this temperature, just below the first-order phase transition at T_{N1}, domains of both phases co-exist within the sample. Nonthermal spin disorder is induced by femtosecond pulses of 1.55-eV light, which reduces the intensity of the x-ray diffraction peak associated with the incommensurate phase less substantially than the peak for the commensurate phase.

VII. CONCLUSIONS

Terahertz time-domain spectroscopy demonstrated that the multiferroic phase is preserved in $Cu_{1-x}Zn_xO$ for $x = 0$, $x = 0.05$. Electromagnons were observed in both pure and alloyed materials, and mode frequencies and widths were relatively insensitive to alloy fraction x. A reduction in the antiferromagnetic ordering temperature was discussed in terms of spin dilution effects. The width of the multiferroic phase increased from 17 K to 30 K on addition of 5% Zn, and infrared and Raman-active phonons weakened and widened. Pronounced changes to the A_u phonon modes occurred in the multiferroic phase in both pure and doped materials, highlighting the direct influence of spin-lattice coupling on this mode. The spin-lattice coupling coefficient was extracted from the temperature dependence of a Raman-active zone-folded LA phonon, and was reduced after spin dilution. Lattice dynamics calculations reproduced the overall reduction in phonon frequencies for $Cu_{0.95}Zn_{0.05}O$ in comparison to CuO.

ACKNOWLEDGMENTS

The authors would like to thank the EPSRC (UK) for financial support, and Dr. D. Walker, M. Dale, and Dr. S. K. Vasheghani Farahani for technical assistance. The Raman and FTIR spectroscopy equipment was funded by the Birmingham and Warwick Science City Research Alliance via Advantage West Midlands (UK) and the European Regional Development Fund (ERDF).

[1] W. Eerenstein, N. D. Mathur, and J. F. Scott, Nature (London) **442**, 759 (2006).
[2] S. W. Cheong and M. Mostovoy, Nat. Mater. **6**, 13 (2007).
[3] S. Y. Yang, J. Seidel, S. J. Byrnes, P. Shafer, C.-H. Yang, M. D. Rossell, P. Yu, Y.-H. Chu, J. F. Scott, J. W. Ager *et al.*, Nat. Nanotechnol. **5**, 143 (2010).
[4] M. Gajek, M. Bibes, S. Fusil, K. Bouzehouane, J. Fontcuberta, A. E. Barthelemy, and A. Fert, Nat. Mater. **6**, 296 (2007).
[5] G. Lawes and G. Srinivasan, J. Phys. D **44**, 243001 (2011).
[6] T. Kimura, T. Goto, H. Shintani, K. Ishizaka, T. Arima, and Y. Tokura, Nature (London) **426**, 55 (2003).
[7] T. Kimura, Y. Sekio, H. Nakamura, T. Siegrist, and A. P. Ramirez, Nat. Mater. **7**, 291 (2008).
[8] X. Rocquefelte, K. Schwarz, P. Blaha, and S. Kumar, Nat. Commun. **4**, 2511 (2013).
[9] H. Katsura, N. Nagaosa, and A. V. Balatsky, Phys. Rev. Lett. **95**, 057205 (2005).
[10] S. Picozzi, K. Yamauchi, I. A. Sergienko, C. Sen, B. Sanyal, and E. Dagotto, J. Phys.: Condens. Matter **20**, 434208 (2008).
[11] A. Pimenov, A. A. Mukhin, V. Y. Ivanov, V. D. Travkin, A. M. Balbashov, and A. Loidl, Nat. Phys. **2**, 97 (2006).
[12] A. Pimenov, T. Rudolf, F. Mayr, A. Loidl, A. A. Mukhin, and A. M. Balbashov, Phys. Rev. B **74**, 100403 (2006).
[13] A. B. Sushkov, R. V. Aguilar, S. Park, S. W. Cheong, and H. D. Drew, Phys. Rev. Lett. **98**, 027202 (2007).
[14] H. Katsura, A. V. Balatsky, and N. Nagaosa, Phys. Rev. Lett. **98**, 027203 (2007).
[15] N. Kida, Y. Takahashi, J. S. Lee, R. Shimano, Y. Yamasaki, Y. Kaneko, S. Miyahara, N. Furukawa, T. Arima, and Y. Tokura, J. Opt. Soc. Am. B-Opt. Phys. **26**, A35 (2009).
[16] A. M. Shuvaev, V. D. Travkin, V. Y. Ivanov, A. A. Mukhin, and A. Pimenov, Phys. Rev. Lett. **104**, 097202 (2010).
[17] V. N. Krivoruchko, Low Temp. Phys. **38**, 807 (2012).
[18] A. Shuvaev, V. Dziom, A. Pimenov, M. Schiebl, A. A. Mukhin, A. C. Komarek, T. Finger, M. Braden, and A. Pimenov, Phys. Rev. Lett. **111**, 227201 (2013).
[19] P. Rovillain, R. de Sousa, Y. Gallais, A. Sacuto, M. A. Measson, D. Colson, A. Forget, M. Bibes, A. Barthelemy, and M. Cazayous, Nat. Mater. **9**, 975 (2010).
[20] M. P. Kostylev, A. A. Serga, T. Schneider, B. Leven, and B. Hillebrands, Appl. Phys. Lett. **87**, 153501 (2005).
[21] S. P. P. Jones, S. M. Gaw, K. I. Doig, D. Prabhakaran, E. Hétroy Wheeler, A. T. Boothroyd, and J. Lloyd-Hughes, Nat. Commun. **5**, 3787 (2014).
[22] A. B. Sushkov, M. Mostovoy, R. Valdés Aguilar, S. W. Cheong, and H. D. Drew, J. Phys.: Condens. Matter **20**, 434210 (2008).
[23] K. Cao, G. C. Guo, and L. X. He, J. Phys.: Condens. Matter **24**, 206001 (2012).
[24] R. Valdés Aguilar, M. Mostovoy, A. B. Sushkov, C.-L. Zhang, Y. J. Choi, S. W. Cheong, and H. D. Drew, Phys. Rev. Lett. **102**, 047203 (2009).
[25] M. Mochizuki, N. Furukawa, and N. Nagaosa, Phys. Rev. Lett. **104**, 177206 (2010).
[26] R. de Sousa and J. E. Moore, Phys. Rev. B **77**, 012406 (2008).
[27] I. Kezsmarki, N. Kida, H. Murakawa, S. Bordacs, Y. Onose, and Y. Tokura, Phys. Rev. Lett. **106**, 057403 (2011).
[28] G. Giovannetti, S. Kumar, A. Stroppa, J. van den Brink, S. Picozzi, and J. Lorenzana, Phys. Rev. Lett. **106**, 026401 (2011).
[29] J. B. Forsyth, P. J. Brown, and B. M. Wanklyn, J. Phys. C: Solid State Phys. **21**, 2917 (1988).

[30] M. Ain, A. Menelle, B. M. Wanklyn, and E. F. Bertaut, J. Phys.: Condens. Matter **4**, 5327 (1992).
[31] M. Ain, W. Reichardt, B. Hennion, G. Pepy, and B. M. Wanklyn, Physica C **162**, 1279 (1989).
[32] D. A. Yablonskii, Physica C **171**, 454 (1990).
[33] F. Wang, T. Zou, Y. Liu, L. Q. Yan, and Y. Sun, J. Appl. Phys. **110**, 054106 (2011).
[34] P. Babkevich, A. Poole, R. D. Johnson, B. Roessli, D. Prabhakaran, and A. T. Boothroyd, Phys. Rev. B **85**, 134428 (2012).
[35] R. Villarreal, G. Quirion, M. L. Plumer, M. Poirier, T. Usui, and T. Kimura, Phys. Rev. Lett. **109**, 167206 (2012).
[36] P. Carretta, F. Cintolesi, and A. Rigamonti, Phys. Rev. B **49**, 7044 (1994).
[37] T. I. Arbuzova, I. B. Smolyak, S. V. Naumov, and A. A. Samokhvalov, Phys. Solid State **40**, 1702 (1998).
[38] C. T. Meneses, J. G. S. Duque, L. G. Vivas, and M. Knobel, J. Non-Cryst. Solids **354**, 4830 (2008).
[39] S. G. Yang, T. Li, B. X. Gu, Y. W. Du, H. Y. Sung, S. T. Hung, C. Y. Wong, and A. B. Pakhomov, Appl. Phys. Lett. **83**, 3746 (2003).
[40] R. A. Borzi, S. J. Stewart, G. Punte, R. C. Mercader, G. A. Curutchet, R. D. Zysler, and M. Tovar, J. Appl. Phys. **87**, 4870 (2000).
[41] P. Shah, A. Gupta, and D. K. Avasthi, Nucl. Instrum. Methods Phys. Res. Sect. B **152**, 343 (1999).
[42] D. Prabhakaran and A. T. Boothroyd, J. Cryst. Growth **250**, 77 (2003).
[43] S. Åsbrink and L. J. Norrby, Acta Crystallogr., Sect. B **26**, 8 (1970).
[44] R. D. Shannon and C. T. Prewitt, Acta Crystallogr., Sect. B **25**, 925 (1969).
[45] R. D. Shannon and C. T. Prewitt, Acta Crystallogr., Sect. B **26**, 1046 (1970).
[46] J. Lloyd-Hughes and T.-I. Jeon, J. Infrared Milli Terahz Waves **33**, 871 (2012).
[47] N. Kida, Y. Yamasaki, R. Shimano, T. Arima, and Y. Tokura, J. Phys. Soc. Jpn. **77**, 123704 (2008).
[48] H. Ohta, S. Okubo, T. Kobayashi, T. Sakurai, W. Zhang, C. Yokoyama, X. G. Zheng, S. Nishihara, K. Inoue, M. Fujisawa *et al.*, IRMMW2012 **1**, 1 (2012).
[49] D. L. Rousseau, R. P. Bauman, and S. P. S. Porto, J. Raman Spectrosc. **10**, 253 (1981).
[50] S. N. Narang, V. B. Kartha, and N. D. Patel, Physica C **204**, 8 (1992).
[51] A. B. Kuz'menko, D. van der Marel, P. J. M. van Bentum, E. A. Tishchenko, C. Presura, and A. A. Bush, Phys. Rev. B **63**, 094303 (2001).
[52] A. B. Kuz'menko, *Reffit software*, http://optics.unige.ch/alexey/reffit.html (2004).
[53] G. Kliche and Z. V. Popovic, Phys. Rev. B **42**, 10060 (1990).
[54] X. K. Chen, J. C. Irwin, and J. P. Franck, Phys. Rev. B **52**, R13130 (1995).
[55] K. Y. Choi, W. J. Lee, A. Glamazda, P. Lemmens, D. Wulferding, Y. Sekio, and T. Kimura, Phys. Rev. B **87**, 184407 (2013).
[56] C. M. Foster, M. Grimsditch, Z. Li, and V. G. Karpov, Phys. Rev. Lett. **71**, 1258 (1993).
[57] A. P. Litvinchuk, A. Möller, L. Debbichi, P. Krüger, M. N. Iliev, and M. M. Gospodinov, J. Phys.: Condens. Matter **25**, 105402 (2013).
[58] B. X. Yang, J. M. Tranquada, and G. Shirane, Phys. Rev. B **38**, 174 (1988).
[59] J. C. Irwin, T. Wei, and J. Franck, J. Phys.: Condens. Matter **3**, 299 (1991).
[60] P. H. Shih, C. L. Cheng, and S. Y. Wu, Nanoscale Res. Lett. **8**, 398 (2013).
[61] M. Kall, A. P. Litvinchuk, L. Borjesson, P. Berastegui, and L. G. Johansson, Phys. Rev. B **53**, 3566 (1996).
[62] H. Y. Xu, Y. C. Liu, C. S. Xu, Y. X. Liu, C. L. Shao, and R. Mu, J. Chem. Phys. **124**, 074707 (2006).
[63] J. B. Wang, H. M. Zhong, Z. F. Li, and W. Lu, J. Appl. Phys. **97**, 086105 (2005).
[64] W. Reichardt, F. Gompf, M. Ain, and B. M. Wanklyn, Z. Phys. B: Condens. Matter **81**, 19 (1990).
[65] V. N. Popov, J. Phys.: Condens. Matter **7**, 1625 (1995).
[66] J. D. Gale, J. Chem. Soc., Faraday Trans. **93**, 629 (1997).
[67] H. Meskine and P. A. Mulheran, Phys. Rev. B **84**, 165430 (2011).
[68] D. Hone, P. A. Montano, T. Tonegawa, and Y. Imry, Phys. Rev. B **12**, 5141 (1975).
[69] C. Dupas and J. P. Renard, Phys. Rev. B **18**, 401 (1978).
[70] A. L. Chernyshev, Y. C. Chen, and A. H. Castro Neto, Phys. Rev. B **65**, 104407 (2002).
[71] T. Edagawa, Y. Fukumoto, and A. Oguchi, J. Magn. Magn. Mater. **310**, E406 (2007).
[72] L. Meddar, M. Josse, P. Deniard, C. La, G. Andre, F. Damay, V. Petricek, S. Jobic, M. H. Whangbo, M. Maglione *et al.*, Chem. Mater. **21**, 5203 (2009).
[73] A. T. Boothroyd, A. Mukherjee, S. Fulton, T. G. Perring, R. S. Eccleston, H. A. Mook, and B. M. Wanklyn, Physica B **234**, 731 (1997).
[74] T. Shimizu, T. Matsumoto, A. Goto, T. V. Chandrasekhar Rao, K. Yoshimura, and K. Kosuge, Phys. Rev. B **68**, 224433 (2003).
[75] C. L. Henley, Phys. Rev. Lett. **62**, 2056 (1989).
[76] S. L. Johnson, R. A. de Souza, U. Staub, P. Beaud, Móhr-Vorobeva, G. Ingold, A. Caviezel, V. Scagnoli, W. F. Schlotter, J. J. Turner *et al.*, Phys. Rev. Lett. **108**, 037203 (2012).